Galinski et al. *NPG Asia Materials* (2019) 11:58
https://doi.org/10.1038/s41427-019-0157-3

NPG Asia Materials

ARTICLE Open Access

Disordered zero-index metamaterials based on metal-induced crystallization

Henning Galinski[1], Andreas Wyss[1], Mattia Seregni[1], Huan Ma[1], Volker Schnabel[1], Alla Sologubenko[1,2] and Ralph Spolenak[1]

Abstract

Zero-index (ZI) materials are synthetic optical materials with a vanishing effective permittivity and/or permeability at a given design frequency. Recently, it has been shown that the permeability of a zero-index host material can be deterministically tuned by adding photonic dopants. Here, we apply metal-induced crystallization (MIC) in quasi-random metal–semiconductor composites to fabricate large-area zero-index materials. Using Ag–Si as a model system, we demonstrate that the localized crystallization of the semiconductor at the metal/semiconductor interface can be used as a design parameter to control light interaction in such a disordered system. The induced crystallization generates new zero-index states corresponding to a hybridized plasmonic mode emerging from selective coupling of light to the Ångstrom-sized crystalline shell of the semiconductor. Photonic doping can be used to enhance the transmission in these disordered metamaterials, as shown by simulations. Our results establish novel large-area zero-index materials for wafer-scale applications and beyond.

Introduction

With the advent of optical metamaterials, numerous new functional materials have emerged that can manipulate electromagnetic (EM) waves in an unprecedented manner. Controlled engineering of the EM properties of materials, represented by their effective permittivity ε and permeability μ, enabled the experimental realization of materials with negative refractive indexes[1,2], flat optics based on plasmonic materials and all dielectric metasurfaces[3,4] and even materials with their real permittivity close to zero[5–9]. Intriguingly, a vanishing permittivity or permeability in such zero-index (ZI) materials leads to new physical regimes of light interaction with matter[10]. ZI materials exhibit quasi-static behavior at optical frequencies, as both the phase velocity $v_p = c/\sqrt{\varepsilon'}$ and/or $v_p = c/\sqrt{\mu'}$ the wavelength λ tend to infinity as the real part of the permittivity ε' or the real part of the permeability μ' approaches zero.

Despite the quasi-static nature of the fields within the ZI material, the dynamics of the field is still that of a transverse wave[11]. The homogenized EM fields and the high impedance mismatch in ZI materials led to considerable theoretical and experimental interest in this matter. Many unconventional phenomena have been predicted in theory, including supercoupling of light through arbitrarily shaped waveguides[12], tunneling of light through subwavelength channels[12–14], wavefront shaping[15,16], electric levitation of nanoscale emitters[17], enhancement of nonlinear optical effects[18], polarization conversion[19], and coherent perfect absorption[20].

Interestingly, even natural materials, such as metals, exhibit ZI behavior, typically in the UV range. This behavior is easily understood by considering the Drude Model[21], which describes the motion of the conduction electrons within a metal stimulated by an external time-harmonic field. In resonance, the real part of the dielectric response $\varepsilon' \approx \varepsilon_c - \omega_p/\omega^2$ vanishes when the oscillating term cancels the contribution of the positively charged metal

Correspondence: Henning Galinski (henning.galinski@mat.ethz.ch) or Ralph Spolenak (ralph.spolenak@mat.ethz.ch)
[1]Laboratory for Nanometallurgy, Department of Materials, ETH Zürich, Zürich, Switzerland
[2]Scientific Center for Optical and Electron Microscopy, ETH Zürich, Zürich, Switzerland

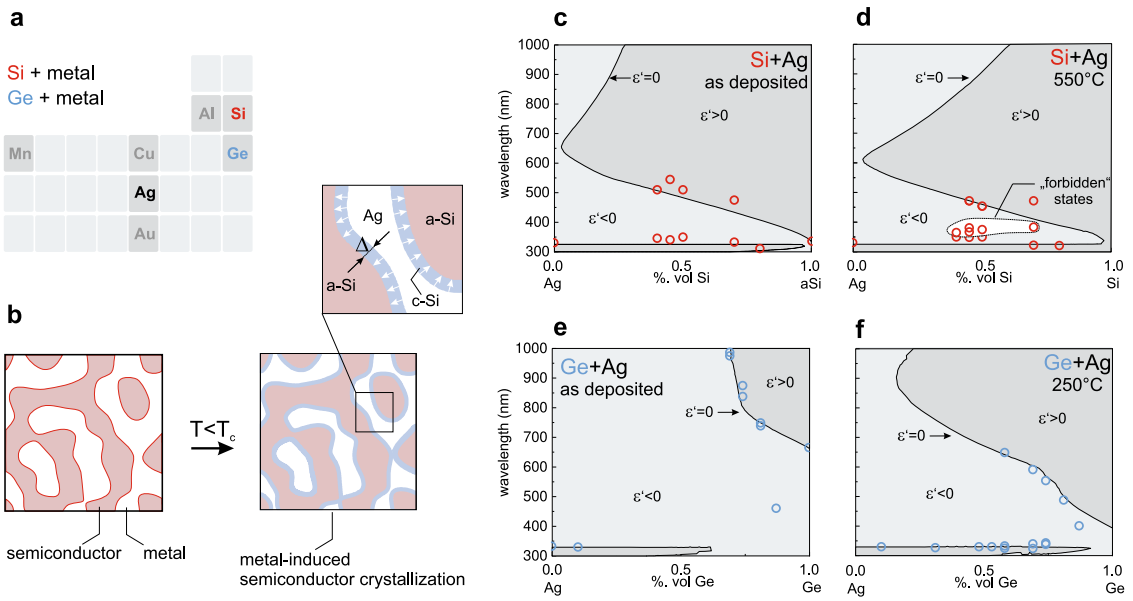

Fig. 1 Designing zero-index materials by metal-induced crystallization. a Selection of immiscible metal/semiconductor pairs. **b** Schematic of metal-induced crystallization in an immiscible metal/semiconductor metamaterial starting from a "phase-separated" state with an amorphous semiconducting phase (red) and crystalline metallic phase (white). After thermal treatment, the semiconductor crystallized (blue) at the metal/semiconductor interface, forming a crystallized layer with thickness Δ. Panels **c**–**f** report near-zero phase diagrams of the as-deposited and arbitrarily chosen annealed states for **c** and **d** Ag–Si and **e** and **f** Ag–Ge. Experimentally determined $\varepsilon' = 0$ states are marked by red (Ag–Si) and blue (Ag–Ge) circles, while the two phases of $\varepsilon' > 0$ and $\varepsilon' < 0$ given by an effective medium approximation are colored in light-blue and gray, respectively. It should be noted that in **d**, "forbidden" states emerge, which go beyond the employed effective medium description

ion cores. At or near this resonance frequency, ZI behavior can be expected. It is noteworthy that ZI behavior, such as large optical nonlinearities[22] or ultrafast optical modulation[23], can only be expected when there is a low optical loss, i.e., when $|\varepsilon| < 1$.

A particularly interesting direction in ZI material research is embedding nonmagnetic inclusions in an epsilon near-zero (ENZ) host medium. This concept was developed in the seminal work by Silveirinha, Liberal, and Engheta[24,25] and enabled engineering of the permeability μ of an ENZ material by only changing the geometric shape or dielectric constant of the introduced inclusions. In this scenario, materials with both ε and μ near zero (EMNZ) can be engineered, and the impedance mismatch between the material and EM radiation from free space is eliminated. Fully near-zero materials are vacuum fluctuation free[26,27] and might serve as a new platform for quantum optics and quantum information. However, a major challenge is the problem of limited scalability. Typically, metamaterials are fabricated using lithography techniques and cannot be scaled above the gram level. It is therefore highly desirable to find new approaches that can transform the conceptional breakthroughs in ZI media to wafer-scale applications.

Here, we use disordered metasurfaces as a new design approach for large-scale ZI media. While usually lacking absolute geometric control, disordered random media can be easily realized on large scales, are polarization independent, and are known to harbor exciting phenomena[28], ranging from wavefront shaping[29], lasing[30], photocatalysis[31], perfect absorption[32], light trapping[33], and circular dichroism[34] to tunable structural coloration[35]. A simple mechanism to engineer a disordered material is phase separation of immiscible phases. When two immiscible materials are mixed together, e.g., oil and water, they instantaneously tend to form separate phases. In solids, this process of phase separation leads to a spatial reorganization of the system, typically accompanied by the formation of quasi-random nanometric patterns.

Considering the special case of an immiscible pair of a metal and a semiconductor (see examples in Fig. 1a), the difference in crystallization temperature of the two materials can lead to a scenario in which the metal phase after phase separation is crystalline while the semiconductor phase remains amorphous. Similar to sintering aids in ceramics, the presence of a metal in an amorphous semiconductor reduces the crystallization temperature and enables preferential crystallization of the semiconductor at the metal/semiconductor interface.

This phenomenon is illustrated in Fig. 1b and commonly dubbed metal-induced crystallization (MIC)[36,37]. As we show below, such spatially localized crystallization furnishes a precise way to engineer the thickness of the crystalline layer by thermal treatments, resulting in a

quasi-random structure with core–shell features reminiscent of nanomatryoshkas[38] or concentric nanorings[39].

Materials and methods

Fabrication

Ag–Ge and Ag–Si ZI films of different compositions were deposited by magnetron sputtering (PVD products). All films were deposited on silica glass under a controlled argon atmosphere of 50 mTorr with a 50 sccm Ar flow. The substrate was kept under a constant rotation of 30 r.p.m. to guarantee a homogeneous composition over the whole substrate. The sputter sources were positioned at 35° with respect to the substrate normal. The base pressure in the sputter tool chamber was $4.0 \pm 1.0 \times 10^{-7}$ Torr. The sources of the deposited material consisted of circular targets with a diameter of 76.2 mm and a thickness of 6.35 mm (MaTeck). The purity of the targets was 99.99% for Ag and 99.999% for Ge and Si.

Prior to sample fabrication, the sputter rate of each individual target/element was determined using AFM and ellipsometry measurements. The deposition rates of Ag, Ge, and Si were 14.5, 14, and 10 nm/min, respectively.

Following deposition, the sputtered substrates were cut into several square-shaped pieces. A piece from each sample batch was annealed in an ultrahigh vacuum oven (RTA system by Createc) at a pressure in the order of 10^{-7} Torr and in the temperature range 100–550 °C. Annealing at such low pressures prevents oxidation of Ag and Si at high temperatures.

Characterization

Ellipsometry

A spectroscopic ellipsometer (M2000-F, J.A. Woollam Co. Inc., Lincoln, NE) was used to measure the optical constants of the films deposited on the silica substrates. All measurements were performed in a wavelength range between 300 and 1000 nm. All the ellipsometry measurements were performed at three different angles of incidence, from 60 to 76° with a 2° angular step. To ensure reproducibility, the dielectric constant was measured at more than two spots per sample.

As far as the measurements of the different compositions of interest are concerned, the model used a 1 mm silica substrate chosen from the software database. The film deposited on top of it was modeled as a subwavelength material that can be treated by an effective permittivity. As initial fitting values, typically Ag or a-Si were chosen. For all data sets, the fitting algorithm enforced the Kramers–Kronig (KK) consistency. The optical constants of the amorphous silicon phase used in the models were taken from a sputtered a-Si calibration sample of known thickness. In a second step, the experimental data were compared to an effective medium model (see Fig. S1 in Supplementary Information).

Energy-dispersive X-ray spectroscopy

The composition of the composites produced was verified by energy-dispersive X-ray spectroscopy (EDS). The device used was an EDAX Apollo X mounted on a ThermoFisher scientific (former FEI) Quanta 200F operated at 20 kV acceleration potential.

Transmission electron microscopy

The in situ and conventional scanning transmission electron microscopy (STEM) and TEM analyses were carried out using a ThermoFisher Scientific (former FEI) Talos F200X operated at 200 kV in both TEM and STEM operation modes. In situ heating studies were performed with a double-tilt DensSolutions heating holder using a DEMS-D6-F-1300-S DensSolutions heating chip with <20-nm-thick SiNx membranes as a supporting foil. The material in this study was sputter deposited onto a chip and studied within membrane areas.

The FFT analyses were performed using TIA software (ThermoFisher Scientific) and compared to the simulated electron diffraction patterns (JEMS software package).

Results

ZI phase diagrams

In our experiments, we started with Ag–Si and Ag–Ge as specific examples of immiscible metal–semiconductor pairs (Fig. 1a). Ag–Si and Ag–Ge thin films with a thickness of 50 nm were codeposited via magnetron cosputtering, and annealing was then performed to begin MIC. Based on the ellipsometric measurements, we derived phase diagrams that contained phases with metallic ($\varepsilon' < 0$) and dielectric ($\varepsilon' > 0$) behavior (Fig. 1c–f). The phase diagrams were based on experimentally determined optical constants of the single elements (see Fig. S1 in Supplementary Information). Therefore, a simple effective medium approximation (EMA) (see Supplementary Information for details) was used to estimate the complex permittivity of the metamaterials and derive the phase diagrams. Figure 1c–f shows different ε'-composition phase diagrams for the as-deposited state and one selected annealing state. In each phase diagram, the experimentally measured ENZ states of the metamaterial are marked for comparison. The phase diagrams are in good agreement with the experimental measurements and reveal ENZ states in the UV and red regions. Quite remarkably, we also observed the formation of forbidden ENZ states, i.e., states not captured by the EMA in the case of the annealed Ag–Si metamaterials (see Fig. 1d). Such states formed for various compositions between 365 and 384 nm. As a good ZI material should satisfy $\varepsilon' \approx 0$ and exhibit low optical losses, i.e., $|\varepsilon| < 1$ (ref. [23]), we concentrated on the Ag–Si system. Detailed information on the Ag–Ge system can be found in the Supplementary Information (Figs. S5 and S6).

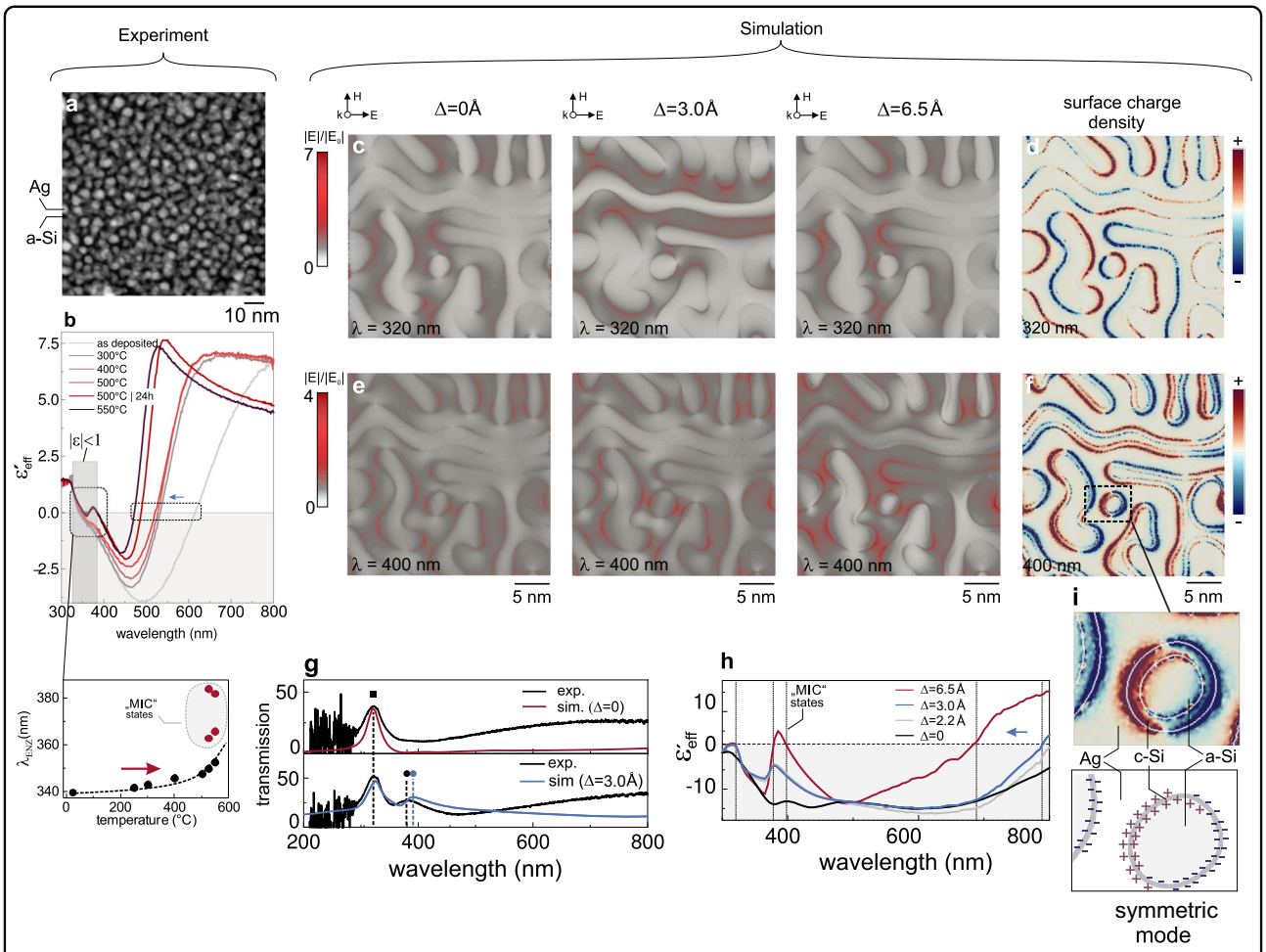

Fig. 2 Optical properties and light interaction. Panel **a** shows an STEM image of an as-deposited AgSi thin film interpenetrating Si (black) and crystalline Ag (gray) phases. **b** Real part of the dielectric function of $Ag_{.55}Si_{.45}$ as a function of thermal treatment. The annealing states (500 and 550 °C) exhibit "MIC-based" ENZ states. The ENZ regime of the metamaterial, i.e., $|\varepsilon| < 1$, is shaded red in gray. **c**–**e** Simulated electric field enhancement for a 50-nm-thick $Ag_{.55}Si_{.45}$ thin film illuminated by a plane wave with the electric field polarized along the *x*-axis at $\lambda_0 = 320$ (**c**) nm and $\lambda_0 = 400$ (**e**) nm. Each panel shows the systems response for a crystalline Si phase of different thickness *Δ*. In the case of **c**, maximal field enhancement (7×) is achieved between adjacent Si-domains, while in **e**, maximal field enhancement (4×) is achieved by coupling to surface-mediated plasmonic modes at the interfaces of the 6.5 Å thick crystalline silicon shells. **d**–**f** Surface charge density of $Ag_{.55}Si_{.45}$ metamaterial with 6.5 Å crystalline shell thickness. **d** The surface charge density distribution is indicative of a collective dipolar mode. **e**–i High charge concentration at the Ag/c-Si and c-Si/a-Si interfaces, causing the formation of a hybridized symmetric mode. **g** Comparison between experimentally measured and simulated transmission spectra for 20-nm-thick metamaterials. **h** Retrieved real part of the permittivity of simulated $Ag_{.55}Si_{.45}$ metasurfaces with different c-Si shell thicknesses *Δ*

Light–matter interaction

We studied the physical mechanisms responsible for the occurrence of these "forbidden" ENZ states by analyzing one selected composition, namely, AgSi, of the Ag–Si metamaterial in detail. Figure 2a shows an STEM micrograph depicting the interpenetrating amorphous Si (black) and crystalline Ag (gray) phases of the metamaterial, confirming the "phase-separated" state of the nanocomposite after deposition. The corresponding EDX maps and spectra are reported in Supplementary Information in Fig. S4. The optical properties, in terms of permittivity, were determined using ellipsometry (Fig. 2). Figure 2b presents the effect of annealing on the real permittivity of this nano-material. A second data set is available in the Supplementary Information in Fig. S3. The spectral response can be subdivided into two spectral regions with characteristic ENZ behaviors.

The first ENZ states, located in the UV and violet regions, combine "forbidden" states and the known Drude–Lorentz response of silver[40]. The latter feature is only weakly dependent on compositional changes and is characterized by a redshift of the critical ENZ wavelength with increasing annealing temperature (Fig. 2b). This trend is easily explained by an on-average increasing dielectric constant of the semiconducting phase. At temperatures ≥500 °C, a new "forbidden" state emerged.

This state is particularly interesting because it is controllable by thermal treatment, which provides a new way to deterministically control the optical response in an overall random and disordered system.

In the second region, located in the red and near IR regions, the spectra show a rich dynamic scenario as the annealing temperature increased. The critical ENZ wavelength continuously blueshifted to decreased wavelengths. However, it must be noted that the losses in this region (see Fig. S2 in Supplementary Information), represented by the imaginary part of the permittivity ε'', in the designed materials are still too high to allow for ENZ behavior. This effect is mostly due to the presence of low-quality amorphous Si, which is characterized by high intrinsic losses compared to those of its crystalline phase. However, these quality issues can be overcome by resorting to ion-beam sputtering or ion-beam-assisted sputtering[41].

To interpret the experimental results, we produced a series of three-dimensional finite element method (FEM) full-wave simulations. We want to stress that our numerical simulations were not intended to replicate the experimental results one-to-one but to derive an intuitive physical picture of the light–matter interaction. To this extent, we built a simplified model of a phase-separated composite using the phase-field method[42]. Our model reproduced the volume fraction and compositional domains of our samples as determined by scanning transmission electron microscopy (Fig. 2(a)). The MIC was modeled by assuming an inward- growing conformal layer on the Si phase. More details on the FEM simulations can be found in the supplementary online text and Fig. S7 in the Supplementary Information.

Figure 2c and e reports the local field enhancement at two ENZ wavelengths, namely, 320 and 400 nm, for different crystalline Si (c-Si) shells. We observed that the coupling of light to the ZI material at these two wavelengths was entirely different. At 320 nm, corresponding to the Drude response, the local electric field enhancement was confined to the nanometer-scale Ag phase due to capacitive coupling between different regions of the Si phase that were independent of the c-Si shell thickness. The coupling abruptly changed at 400 nm, where the light was tightly confined to the interfaces of the Ångstrom-sized c-Si shell of the metasurface. We used the effective parameter retrieval method[43] to assess the effective permittivity of the simulated ZI materials. The quantitative prediction of our FEM model shown in Fig. 2h reproduced the formation of the "MIC-based" near-zero state and exhibited all the characteristic features that were also found in the experiment, as shown in Fig. 2b. The observed redshift between the simulated and experimental near-zero states can be attributed to the known influence of the particle aspect ratio on plasmonic resonances[44]. Due to the periodic boundary condition used in the simulation, we artificially truncated the phases of our material and thus systematically underestimated their aspect ratio.

To further analyze the properties of "MIC-based" near-zero states, we mapped the surface charge density in the case of $\Delta = 6.5$ Å, as shown in Fig. 2d and f. While the near-zero state at 320 nm was characterized by a classical collective plasmonic dipolar mode of the material with quasi-uniform field in the semiconductor, the MIC-based state emerges due to coupling of local symmetric modes, where charges primarily reside on the inner and outer interfaces of the crystalline Si shell (Fig 2i). In the experiment as well as the simulation, this mode caused enhanced transmission in the far field, as shown in Fig. 2g. This phenomenon can be understood in the context of optical cloaking in core–shell nanoparticles[45–49]. As analyzed by Kerker[45,46] and others[47,48], the polarizability, i.e., the scattering of concentric spheres of properly chosen permittivity ($\varepsilon_{\mathrm{core}} < \varepsilon_{\mathrm{medium}} < \varepsilon_{\mathrm{shell}}$), becomes zero for a critical shell thickness, which occurs when the scattered waves produced by the dipolar resonances of the inner and outer shell destructively interfere. Invisibility, i.e., the complete suppression of light scattering in this frequency range, is achieved for specific ratios of the core r_{core} and total radius r of the particle[46,47]. Neeves and Birnboim[50] derived the condition for a surface-mediated plasmon resonance for such a core–shell particle suspended in a third medium. The resonance condition is given by

$$Re(\varepsilon_{shell}[\varepsilon_{core}(3-2P)+2\varepsilon_{shell}P]+2\varepsilon_{medium}[\varepsilon_{core}P+\varepsilon_{shell}(3-P)])=0 \quad (1)$$

and can be tuned by adjusting $P = 1-(r_{core}/r_{shell})^3$, i.e. the ratio of the core to the shell radius, see for example[51].

Here, we created a similar phenomenon in a disordered system. Modulating the subnanometer thickness of the crystalline Si shell by the temperature generated a hybridized "ENZ"-resonance state that effectively coupled incoming radiation to the interfaces of the crystalline Si shell. These local plasmonic resonances did not propagate into the far field and therefore successfully suppressed the material scattering response. It should be noted that the experimental realization of such picocavities[52] represents a new and practical way to study the extreme-coupling regime where the classical model of electron response is known to fail[53].

In situ MIC

To study and validate the crystallization of semiconducting phase domains adjacent to the metallic phase in the experiment, we used to in situ transmission electron microscopy. Figure 3b, c shows a metal-dielectric composite composed of subwavelength Ag nanoparticles

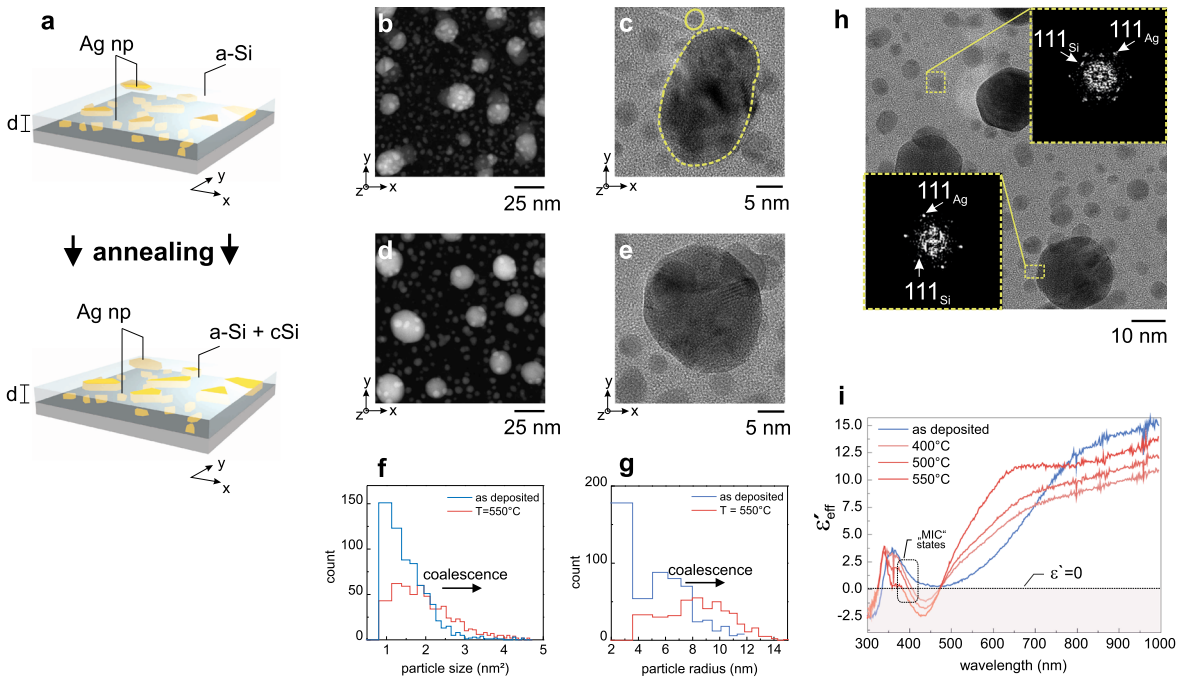

Fig. 3 Optical properties and morphology of Ag–Si-based ENZ materials by metal-induced crystallization. a Schematic presenting the morphology of immiscible Ag–Si thin films before and after annealing as determined from TEM measurements. **b**–**e** STEM and TEM micrographs of a pristine $Ag_{.30}Si_{.70}$ sputtered onto an **b**, **c** SiN membrane and **d**, **e** after in situ annealing at 550 °C for 20 min. Panels **f** and **g** compare the particle size distribution of **f** small and **g** large Ag nanoparticles before and after annealing at 550 °C. **h** High-resolution TEM micrograph of the in situ annealed specimen with a corresponding fast Fourier transforms acquired from the marked areas at Ag particles. **i** Real part of the calculated dielectric function of $Ag_{.30}Si_{.70}$ as a function of thermal treatment

(Ag-nP) embedded in the amorphous Si matrix. The Ag-nP population exhibits a bimodal size distribution (Fig. 3f, g) that is stable during annealing up to C, as confirmed by direct observation during in situ heating in the transmission electron microscope. Only marginal coarsening and particle growth were detected by the postmortem analysis of the micrographs (Fig. 3d, e).

Fast Fourier transform (FFT) analysis of the micrographs acquired during the in situ heating experiments demonstrated the occurrence of the crystalline Si phase exclusively at the perimeters of the small and large Ag particles (see Fig. 3h). Such an occurrence was never detected in the nonheat-treated material. The localized crystallization of the Si at the Ag particles correlates with the observed optical response due to the formation of MIC-based states (Fig. 3i).

Photonic doping

As demonstrated above, a dynamic optical response with $\varepsilon \approx 0$ can be created by exploiting the concepts of phase separation and MIC in metal–semiconductor mixtures. An intriguing question concerns the possibility of reducing material-specific losses in these systems to design a class of metamaterials with $\varepsilon \approx 0$ and $\mu \approx 0$ behavior. As shown recently by Liberal et al., ε and μ near-zero behavior can be realized by photonic doping, i.e., the introduction of dielectric nanorods or similar materials. To theoretically study the possibility of "photonic doping" in MIC-based ENZ materials, we produced a series of finite element (FE) simulations. We employed two-dimensional simulations based on the measured permittivity of a $Ag_{.55}Si_{.45}$ thin film annealed at 550 °C. Figure 4a reports the interaction of a TM plane wave under normal incidence with a 150 nm $Ag_{.55}Si_{.45}$ thin film.

The computed magnetic field shown in Fig. 4a exhibited a constant magnetic field within the $Ag_{.55}Si_{.45}$ thin film, confirming the characteristic ENZ behavior. Doping the ENZ host material with dielectric rods and dielectric particles made of TiO_2, as shown in Fig. 4b, c, results in either an enhanced or a highly reduced transmission, as shown in Fig. 4d, e. This is a very important result, as it confirms that the MIC-based thin films can serve as ENZ host materials whose material properties can be further modulated by photonic doping. Interestingly, the optical response of the doped ENZ material exhibits the unique features of a Fano resonance[54]. In particular, the field distribution and the fact that the optical response can be switched by geometrical means from high to low transmission are reminiscent of a Fano response in dielectric resonators[55].

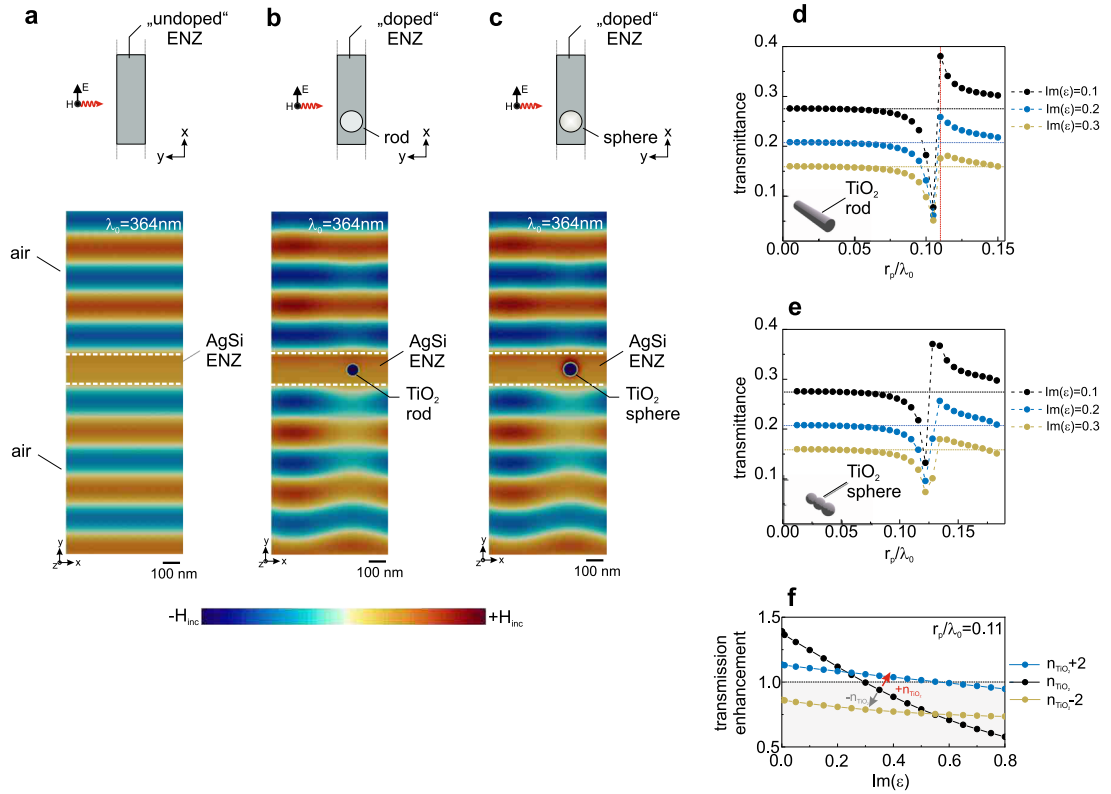

Fig. 4 Photonic Doping a Schematic of the undoped Ag–Si ENZ host and simulated magnetic field magnitude distribution for a 150-nm-thick ENZ slab illuminated by a plane wave with the magnetic field polarized along the *z*-axis at $\lambda_0 = 364$ nm. **b** and **c** same as in **a**, but the ENZ slab was doped with **b** dielectric TiO_2 rods and **c** dielectric TiO particles ($\varepsilon = 13.4$). Panels **d** and **e** show the magnitude of the transmission coefficient as a function of the **d** rod or **e** particle radius r_p/λ_0 for three different loss values Im(ε). In both cases, the overall transmission can be enhanced by using either a rod or particle once the radius r_p reaches a critical size. **f** Transmission enhancement for TiO rods as a function of the optical losses, i.e., Im(ε), in the ENZ matrix

In addition to its geometrical dependence, the transmission enhancement also depends on the optical losses of the ENZ matrix. We numerically verified this effect, as shown in Fig. 4f, by simulating the transmission enhancement for a given r_p/λ_0 value as a function of the optical losses, i.e., Im(ε) of the ENZ matrix. For a TiO rod dispersed in an ENZ matrix, the transmission enhancement vanished for Im(ε) > 0.3. Interestingly, by changing the refractive index of the TiO particle, it can be seen in Fig. 4f that the maximal tolerable loss for the ENZ host material depended on the permittivity of the dopant as well. Thus, one can, in principle, relax the requirement for low optical losses by choosing dielectric dopants with an elevated refractive index.

Discussion

In this article, we designed, fabricated, and characterized disordered optical metamaterials with vanishing permittivity consisting of immiscible metal–semiconductor pairs. We demonstrated that MIC can be used to engineer a set of new near-zero states in such disordered quasi-random metamaterials. These near-zero states emerged due to the formation of a temperature-controllable Ångström-sized crystalline silicon (c-Si) shell in the Ag–Si metamaterial. We showed that near-zero states are the result of a collective resonance, where light is confined to an ångström-sized c-Si shell by a mechanism analogous to optical cloaking in concentric core–shell nanoparticles. This demonstration of controlled coupling of light to Ångström-sized volumes in a disordered system represents a tremendous opportunity to study the extreme-coupling regime in robust and scalable disordered optical media. Using simulations, we demonstrated that the near-zero response of such a large-area metamaterial can be further modulated by photonic doping to create a full ZI response. As the proposed disordered metamaterials were fabricated by simple deposition methods and were not constrained with respect to their active area, we expect that these ideas can be exploited to design ZI media for wafer-scale applications of integrated photonics, thermal sensors, and quantum information.

Acknowledgements

This work was supported by ETH Research Grant ETH-47 18-1. The authors thank the Scientific Center for Optical and Electron Microscopy (ScopeM) and the FIRST cleanroom team at the ETH Zurich for their support. We thank N.

Spencer and the LSST for access to the ellipsometer. Some of the calculations reported here were performed using the BRUTUS cluster at ETH Zurich.

Author details
[1]Laboratory for Nanometallurgy, Department of Materials, ETH Zürich, Zürich, Switzerland. [2]Scientific Center for Optical and Electron Microscopy, ETH Zürich, Zürich, Switzerland

Author contributions
H.G. and A.W. designed the study. M.S. and V.S. fabricated the samples used in the article. M.S. and H.G. performed the optical measurements. H.G., A.W., and M.S. analyzed the optical measurements. A.W. performed the Raman measurements. V.S. and H.M. performed the XRD measurements. A.S. performed and analyzed the in situ TEM/STEM measurements. H.G. wrote the manuscript. H.G. designed the theoretical research, developed, and performed the FEM simulations. R.S. suggested experiments and contributed to the interpretation. All authors contributed equally to the preparation of the manuscript.

Conflict of interest
The authors declare that they have no conflict of interest.

Supplementary information is available for this paper at https://doi.org/10.1038/s41427-019-0157-3.

Received: 9 May 2019 Revised: 11 June 2019 Accepted: 3 July 2019.
Published online: 18 October 2019

References

1. Shelby, R. A., Smith, D. R. & Schultz, S. Experimental verification of a negative index of refraction. *Science* **292**, 77–79 (2001).
2. Zhang, S. et al. Experimental demonstration of near-infrared negative-index metamaterials. *Phys. Rev. Lett.* **95**, 137404, https://doi.org/10.1103/PhysRevLett.95.137404 (2005).
3. Yu, N. et al. Light propagation with phase discontinuities: generalized laws of reflection and refraction. *Science* **334**, 333–337 (2011).
4. Chen, W. T. et al. A broadband achromatic metalens for focusing and imaging in the visible. *Nat. Nanotechnol.* **13**, 220–226, https://doi.org/10.1038/s41565-017-0034-6 (2018).
5. Maas, R., Parsons, J., Engheta, N. & Polman, A. Experimental realization of an epsilon-near-zero metamaterial at visible wavelengths. *Nat. Photonics* **7**, 907–912, https://doi.org/10.1038/nphoton.2013.256 (2013).
6. Liu, R. et al. Experimental demonstration of electromagnetic tunneling through an epsilon-near-zero metamaterial at microwave frequencies. *Phys. Rev. Lett.* **100**, 023903, https://doi.org/10.1103/PhysRevLett.100.023903 (2008).
7. Adams, D. C. et alFunneling light through a subwavelength aperture with epsilon-near-zero materials. *Phys. Rev. Lett.* **107**, 133901, https://doi.org/10.1103/PhysRevLett.107.133901 (2011).
8. Caspani, L. et al. Enhanced nonlinear refractive index in ε-near-zero materials. *Phys. Rev. Lett.* **116**, 233901, https://doi.org/10.1103/PhysRevLett.116.233901 (2016).
9. Kim, J. et al. Role of epsilon-near-zero substrates in the optical response of plasmonic antennas. *Optica* **3**, 339–346 (2016).
10. Engheta, N. Pursuing near-zero response. *Science* **340**, 286–287 (2013).
11. Ziolkowski, R. W. Propagation in and scattering from a matched metamaterial having a zero index of refraction. *Phys. Rev. E* **70**, 046608, https://doi.org/10.1103/PhysRevE.70.046608 (2004).
12. Silveirinha, M. G. & Engheta, N. Theory of supercoupling, squeezing wave energy, and field confinement in narrow channels and tight bends using ε near-zero metamaterials. *Phys. Rev. B* **76**, 245109, https://doi.org/10.1103/PhysRevB.76.245109 (2007).
13. Silveirinha, M. & Engheta, N. Tunneling of electromagnetic energy through subwavelength channels and bends using ε-near-zero materials. *Phys. Rev. Lett.* **97**, 157403, https://doi.org/10.1103/PhysRevLett.97.157403 (2006).
14. Inampudi, S. et al. Enz-enhanced transmission through subwavelength slits. In *CLEO: 2011—Laser Science to Photonic Applications*, 1–2 https://doi.org/10.1364/CLEO_AT.2011.JTuI56 (Oxford, UK, 2011).
15. Alù, A., Silveirinha, M. G., Salandrino, A. & Engheta, N. Epsilon-near-zero metamaterials and electromagnetic sources: tailoring the radiation phase pattern. *Phys. Rev. B* **75**, 155410, https://doi.org/10.1103/PhysRevB.75.155410 (2007).
16. A. S. Shalin, et al. Optical cloaking with enz-metamaterials. In *2015 9th International Congress on Advanced Electromagnetic Materials in Microwaves and Optics (METAMATERIALS)*, 487–489 (Oxford, UK, 2015).
17. Rodríguez-Fortuño, F. J., Vakil, A. & Engheta, N. Electric levitation using Ïµ-near-zero metamaterials. *Phys. Rev. Lett.* **112**, 033902, https://doi.org/10.1103/PhysRevLett.112.033902 (2014).
18. Argyropoulos, C., Chen, P.-Y., D'Aguanno, G., Engheta, N. & Alù, A. Boosting optical nonlinearities in ε-near-zero plasmonic channels. *Phys. Rev. B* **85**, 045129, https://doi.org/10.1103/PhysRevB.85.045129 (2012).
19. Ginzburg, P. et al. Manipulating polarization of light with ultrathin epsilon-near-zero metamaterials. *Opt. Express* **21**, 14907–14917, (2013).
20. Feng, S. & Halterman, K. Coherent perfect absorption in epsilon-near-zero metamaterials. *Phys. Rev. B* **86**, 165103, https://doi.org/10.1103/PhysRevB.86.165103 (2012).
21. U. Mizutani. *Introduction to Electron Theory of Metals* (Cambridge University Press, Cambridge, UK, 2001).
22. Alam, M. Z., De Leon, I. & Boyd, R. W. Large optical nonlinearity of indium tin oxide in its epsilon-near-zero region. *Science* **352**, 795–797 (2016).
23. Kinsey, N. et al. Epsilon-near-zero al-doped zno for ultrafast switching at telecom wavelengths. *Optica* **2**, 616–622 (2015).
24. Silveirinha, M. & Engheta, N. Design of matched zero-index metamaterials using nonmagnetic inclusions in epsilon-near-zero media. *Phys. Rev. B* **75**, 075119, https://doi.org/10.1103/PhysRevB.75.075119 (2007).
25. Liberal, I., Mahmoud, A. M., Li, Y., Edwards, B. & Engheta, N. Photonic doping of epsilon-near-zero media. *Science* **355**, 1058–1062 (2017).
26. Liberal, I. & Engheta, N. Zero-index structures as an alternative platform for quantum optics. *Proc. Natl Acad. Sci. USA* **114**, 822–827 (2017).
27. Biehs, S.-A. & Agarwal, G. S. Qubit entanglement across ε-near-zero media. *Phys. Rev. A* **96**, 022308, https://doi.org/10.1103/PhysRevA.96.022308 (2017).
28. Wiersma, D. S. Disordered photonics. *Nat. Photon.* **7**, 188, https://doi.org/10.1038/nphoton.2013.29 (2013).
29. Jang, M. et al. Wavefront shaping with disorder-engineered metasurfaces. *Nat. Photonics* **12**, 84–90, https://doi.org/10.1038/s41566-017-0078-z (2018).
30. Wiersma, D. S. The physics and applications of random lasers. *Nat. Phys.* **4**, 359, https://doi.org/10.1038/nphys971 (2008).
31. Y. Tian, et al. Enhanced solar-to-hydrogen generation with broadband epsilonâ€ nearâ€ zero nanostructured photocatalysts. *Adv. Mater.* **29**, 1701165. https://doi.org/10.1002/adma.201701165.
32. Galinski, H., Fratalocchi, A., Döbeli, M. & Capasso, F. Light manipulation in metallic nanowire networks with functional connectivity. *Adv. Opt. Mater.* **5**, 1600580 (2017).
33. Lee, W.-K. et al. Concurrent design of quasi-random photonic nanostructures. *Proc. Natl Acad. Sci. USA* **114**, 8734–8739 (2017).
34. Fasold, S.et al. Disorder-enabled pure chirality in bilayerplasmonic metasurfaces. *ACS Photonics* **5**, 1773–1778, https://doi.org/10.1021/acsphotonics.7b01460 (2018).
35. Galinski, H. et al. Scalable, ultra-resistant structural colors based on network metamaterials. *Light Sci. Appl.* **6**, e16233, https://doi.org/10.1038/lsa.2016.233 (2017).
36. Z. Wang, L. P. Jeurgens & E. J. Mittemeijer. *Metal-Induced Crystallization: Fundamentals and Applications* (CRC Press, New York, NY, 2015).
37. Z. Wang, L. P. H. Jeurgens, J. Y. Wang & E. J. Mittemeijer. Fundamentals of metal-induced crystallization of amorphous semiconductors. *Adv. Eng. Mater.* **11**, 131–135. https://onlinelibrary.wiley.com/doi/abs/10.1002/adem.200800340 (2009).
38. Bardhan, R. et al. Nanosphere-in-a-nanoshell: a simple nanomatryushka. *J. Phys. Chem. C* **114**, 7378–7383, https://doi.org/10.1021/jp9095387 (2010).
39. Alaee, R. et al. Scattering dark states in multiresonantconcentric plasmonic nanorings. *ACS Photonics* **2**, 1085–1090, https://doi.org/10.1021/acsphotonics.5b00133 (2015).
40. Yang, H. U. et al. Optical dielectric function of silver. *Phys. Rev. B* **91**, 235137, https://doi.org/10.1103/PhysRevB.91.235137 (2015).

41. Murray, P. G. et al. Ion-beam sputtered amorphous silicon films for cryogenic precision measurement systems. *Phys. Rev. D.* **92**, 062001, https://doi.org/10.1103/PhysRevD.92.062001 (2015).
42. Zhu, J., Lu, X., Balieu, R. & Kringos, N. Modelling and numerical simulation of phase separation in polymer modified bitumen by phase-field method. *Mater. Des.* **107**, 322–332 (2016).
43. Smith, D. R., Vier, D. C., Koschny, T. & Soukoulis, C. M. Electromagnetic parameter retrieval from inhomogeneous metamaterials. *Phys. Rev. E* **71**, 036617, https://doi.org/10.1103/PhysRevE.71.036617 (2005).
44. Maier, S. A. *Plasmonics: Fundamentals and Applications* (Springer Science & Business Media, New York, NY, 2007).
45. Kerker, M. Invisible bodies. *J. Opt. Soc. Am.* **65**, 376–379 (1975).
46. Kerker, M. Lorenz-mie scattering by spheres: Some newly recognized phenomena. *Aerosol Sci. Technol.* **1**, 275–291, https://doi.org/10.1080/02786828208958594 (1982).
47. Alù, A. & Engheta, N. Achieving transparency with plasmonic and metamaterial coatings. *Phys. Rev. E* **72**, 016623, https://doi.org/10.1103/PhysRevE.72.016623 (2005).
48. Rohde, C., Hasegawa, K. & Deutsch, M. Plasmon-assisted transparency in metal-dielectric microspheres. *Opt. Lett.* **32**, 415–417 (2007).
49. Mühlig, S. et al. A self-assembled three-dimensional cloak in the visible. *Sci. Rep.* **3**, 2328, https://doi.org/10.1038/srep02328 (2013).
50. Neeves, A. E. & Birnboim, M. H. Composite structures for the enhancement of nonlinear-optical susceptibility. *J. Opt. Soc. Am. B* **6**, 787–796 (1989).
51. Alú, A. & Engheta, N. Polarizabilities and effective parameters for collections of spherical nanoparticles formed by pairs of concentric double-negative, single-negative, and/or double-positive metamaterial layers. *J. Appl. Phys.* **97**, 094310, https://doi.org/10.1063/1.1884757 (2005).
52. J. J. Baumberg, J. Aizpurua, M. H. Mikkelsen & D. R. Smith. Extreme nanophotonics from ultrathin metallic gaps. *Nat. Mater.* 1 (2019).
53. Ciracì, C. et al. Probing the ultimate limits of plasmonic enhancement. *Science* **337**, 1072–1074 (2012).
54. Limonov, M. F., Rybin, M. V., Poddubny, A. N. & Kivshar, Y. S. Fano resonances in photonics. *Nat. Photonics* **11**, 543, https://doi.org/10.1038/nphoton.2017.142 (2017).
55. Rybin, M. V. et al. Switchable invisibility of dielectric resonators. *Phys. Rev. B* **95**, 165119, https://doi.org/10.1103/PhysRevB.95.165119 (2017).